

Predictive Energy Management for Hybrid Powertrains

Satish Vedula, and Olugbenga Moses Anubi

Department of Electrical and Computer Engineering, the Center for Advanced Power Systems, Florida State University E-mail: {svedula, oanubi}@fsu.edu

COPYRIGHTED. Submitted to IFAC MECC 2026 and ASME Letters in Dynamic Systems and Control Joint Submission (Under Review)

1 Abstract

Hybrid power trains (HPT) run on multiple energy sources, often involving energy storage systems/batteries (ESS). As a result, the risk of battery degradation and the reliability of energy storage elements pose a major challenge in designing an energy-efficient hybrid power train. This paper presents an energy management strategy that adaptively splits power demand between the engine and the battery pack in a hybrid power train taking into account the battery degradation. Incorporating the battery degradation model directly into the underlying optimization problem is challenging on multiple fronts: 1) Any reasonable degradation model will, due to its complexity, result in a complicated optimization problem that is impractical for real-time implementation 2) the models contain a lot of time-varying parameters that can only be determined through destructive experimental procedures. As a result, it is essential to devise heuristics that reasonably capture the degradation per usage of the batteries. One such heuristic considered in this paper is the absolute power extracted from the battery. A distributed model predictive strategy is then developed to coordinate the power split to maximize efficiency while mitigating the failure risk due to battery degradation. The designed EM strategy is demonstrated through a realistic simulation of three different hybrid power trains: hybrid road vehicles (for example: a hybrid electric vehicle (HEV)), hybrid surface vehicles (for example: dynamically positioned hybrid ships (DPS)), and hybrid aerial vehicles (for example: hybrid electric aircraft (HEA)). The results show the effectiveness of the energy management strategy in managing battery degradation.

2 Introduction

An HPT comprises multiple forms of energy-generating sources namely: engine and battery. Over the years hybridization of traditional power trains has broadened across all manufacturing industries for example automobile industry (hybrid electric vehicles), the naval and shipping industry (hybrid electric ships), and the aviation industry (hybrid electric aircraft). As mentioned, one such example of an HPT is a hybrid electric vehicle (HEV). Stringent regulations on environmental emissions and the impending extreme limitations on the consumption of oil and gas products are prompting the automotive industry to shift focus to more alternate-energy-dependent vehicles such as fuel cell hybrid vehicles (FHV), battery Electric vehicles (BEVs) and hybrid electric vehicles (HEVs) [1]. Optimal energy management (EM) between engine and battery plays a pivotal role in enhancing the fuel efficiency of HEV, but achieving it is extremely challenging due to the changing modes of operation of HEV. Rule-based Control (RBC) is one of the HEV EM methods that gained traction during the inception of HEVs [2]. However, it is often difficult to encapsulate and capture all the system attributes into RBC to facilitate seamless operation. As a result, enhancements in computational devices have led to a substantial increase in the use of optimization-based methods such as model predictive control (MPC) [3][4], reinforcement learning (RL) [5][6].

Improvement of fuel economy and range extension are two of the major key performance indicators in the EM of HEVs, with cost functions defined in the objective of MPC problem to consider fuel injection and efficient engine operation. Numerous investigators have proposed algorithms that made fuel minimization a key part of the optimization problem [3, 4, 7, 8, 9, 10, 11]. However, it is a well-known fact that the batteries degrade faster than the engines. Thus, it is important to prescribe optimization problems that consider fuel consumption while simultaneously managing battery degradation.

Related existing approaches have considered both fuel minimization and battery management in designing an EM for HEV [12, 13, 14, 15, 16, 17, 18]. In [12], the authors propose an adaptive MPC for EM of HEV and validate the control through a real-time hardware in loop (HIL) test. The state of charge (SoC) of the battery was regulated around a set-point value, but the impact of this EM design on the battery's health was not considered. In [13] the authors incorporated both the battery thermal and degradation models via the so-called *coulomb counting* in their proposed EM strategy. In their work, the impact of the designed EM on battery health was studied. However, the driving duration considered was around 2 hours, which is insufficient to understand the effect of the battery degradation completely. In [14][18] the battery state of health (SoH) model is used directly in the optimization to minimize the battery degradation. However, due to the complex dynamics of the battery capacity function, it is difficult to estimate the battery capacity in order to minimize the degradation. In [16], the authors chose to minimize battery power to slow down the battery degradation. However, the approach taken is based on Pontryagin's minimum principle in which not all the system constraints were able to be accounted

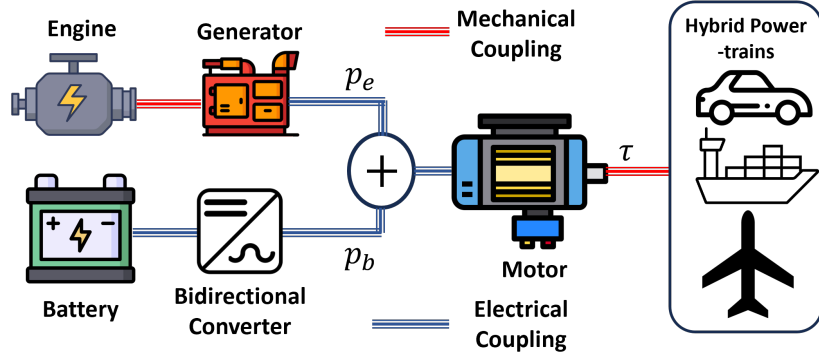


Figure 1: Hybrid power-train schematic with different applications to road vehicles (hybrid electric cars), surface vehicles (dynamically positioned ships), and aerial vehicles (hybrid electric aircraft).

for. Also, the simulation duration of 200 seconds is insufficient to capture the complex degradation mechanism.

Dynamically positioned hybrid ships as a case study of a hybrid power train, and studying the load split is carried out by numerous researchers in the existing literature [19, 20, 21, 22, 23]. Similarly, hybrid electric aircraft as an example of the hybrid power train is also carried out by few researchers in the existing literature [24, 25, 26]. However, the impact of battery degradation was not explicitly considered in the existing approaches for both dynamically positioned hybrid ships and hybrid electric aircraft. The key contributions in this work are:

1. A generalized Euler-Lagrange-based model is presented for HPTs with an example of Road vehicles, Surface vehicles, and Ariel vehicles.
2. A model predictive energy management strategy considering a heuristic to minimize the battery power, thus minimizing the battery degradation and the efficient operation of the engine around an operating point. Fig. 2 shows the overall developed framework.
3. A scalable plug-and-play distributed framework is developed, which can be applied to hybrid power trains consisting of n number of power sources.
4. Realistic simulation experiments are conducted using real drive-cycle data from the U.S. Environment and Protection Agency (EPA) to mimic long-range driving (360 hours) for hybrid electric vehicles and capture evolutionary trends for battery degradation. This demonstrates the effect of the designed model predictive energy management strategy in achieving stated objectives. Similar simulations are performed for dynamically positioned hybrid ships and hybrid electric aircraft.

5. A *real-time* target simulation of the proposed algorithm in testing the algorithm's real-time capabilities via three test cases of a hybrid electric vehicle, dynamically positioned hybrid ship, and hybrid electric aircraft.

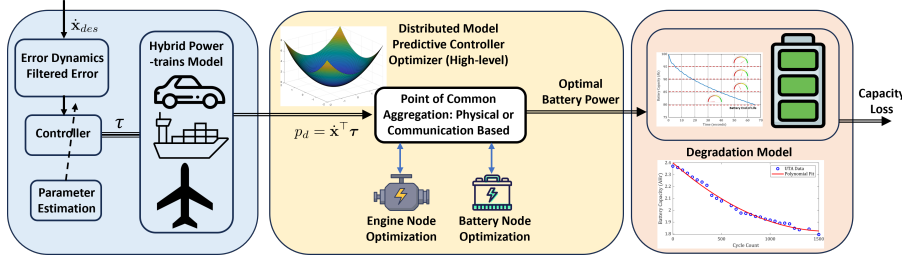


Figure 2: Distributed optimization implementation scheme

The rest of the paper is organized as follows: In Section-3, the mathematical notations used throughout the paper are presented. Section-4 contains the model development of the battery and the drive-line dynamics. In Section-4, the proposed distributed battery health aware model predictive energy management (MPEM) is developed. In Section-7, the developed EM controller is tested via a realistic simulation of the developed model, and the results are presented and discussed. Finally, the conclusions are presented in Section-8.

3 Notations

The set of natural numbers is represented by \mathbb{N} and the set of real numbers denoted by \mathbb{R} . A matrix with n rows and m columns is denoted as $\mathbb{R}^{n \times m}$. \mathbb{R}_+ denotes the set of positive real numbers. \mathbb{L}_2 and \mathbb{L}_∞ denote the square-integrable (measurable) and bounded signal spaces. Scalars are denoted by lowercase alphabets (for example $x \in \mathbb{R}$ and $y \in \mathbb{N}$). The notation $\mathcal{P} \subset \mathbb{R}^n$ represents polytopes of the form $\{\mathbf{x} \in \mathbb{R}^n | A_i \mathbf{x}_i \preceq \mathbf{b}_i, A_e \mathbf{x} = \mathbf{b}_e\}$, where the parameters $A_e, \mathbf{b}_e, A_i, \mathbf{b}_i$ can be inferred from problem specific context. Real vectors are represented by the lowercase bold alphabets (i.e. $\mathbf{x} \in \mathbb{R}^n$). The vector of ones is denoted as $\mathbf{1}$. The vector of zeros is denoted as $\mathbf{0}$. $I_n \in \mathbb{R}^{n \times n}$ denotes the identity matrix of dimension n . For any vector $\mathbf{x} \in \mathbb{R}^n$, $\|\mathbf{x}\|_2 \triangleq \sqrt{\mathbf{x}^\top \mathbf{x}}$, represents the 2-norm. The symbol \preceq denotes the component-wise inequality i.e. $\mathbf{x} \preceq \mathbf{y}$ is equivalent to $\mathbf{x}_i \leq \mathbf{y}_i$ for $i = 1, 2, \dots, n$.

4 Model Development

The hybrid power-train considered in this paper, shown in Fig. 1, is a parallel interconnection of two energy pathways – one consisting of a unidirectional engine/generator source, while the other is a bidirectional storage/converter resource. This interconnection supplies an electric motor which is a prime mover

for the vehicle dynamics. As shown in the figure, this architecture is applicable to a wide variety of modalities including road vehicles, surface vehicles, and aerial vehicles. To this effect, the generalized vehicle dynamics is given by the Euler-Lagrange dynamics [27]

$$M(\mathbf{x})\ddot{\mathbf{x}} + V_m(\mathbf{x}, \dot{\mathbf{x}})\dot{\mathbf{x}} + G(\mathbf{x}) + F(\dot{\mathbf{x}}) = \boldsymbol{\tau}, \quad (1)$$

where $\mathbf{x}(t), \dot{\mathbf{x}}(t) \in \mathbb{R}^n$ are the generalized position and velocity respectively, $M(\mathbf{x}) \in \mathbb{R}^{n \times n}$ denotes the inertia matrix, $V_m(\mathbf{x}, \dot{\mathbf{x}}) \in \mathbb{R}^{n \times n}$ the centripetal-Coriolis matrix, $G(\mathbf{x}) \in \mathbb{R}^{n \times n}$ the gravity vector, $F(\dot{\mathbf{x}}) \in \mathbb{R}^{n \times n}$ the generalized damping torque, and $\boldsymbol{\tau} \in \mathbb{R}^n$ generalized torque input. The dynamics in (1) is well known [28] to satisfy the following properties which are used for subsequent control development:

1. There exists positive real numbers $m_2 > m_1 > 0$ such that $m_1 \|\mathbf{z}\|^2 \leq \mathbf{z}^\top M(\mathbf{x})\mathbf{z} \leq m_2 \|\mathbf{z}\|^2$ for all $\mathbf{x}, \mathbf{z} \in \mathbb{R}^n$
2. The skew symmetric property $\mathbf{z}^\top \left(\dot{M}(\mathbf{x}) - \frac{1}{2}V_m(\mathbf{x}, \dot{\mathbf{x}}) \right) \mathbf{z} = 0$ holds for all $\mathbf{x}, \mathbf{z} \in \mathbb{R}^n$,
3. *Linear Parametrization:* For a continuously differentiable trajectory given by the stable dynamics $\dot{\mathbf{x}}_d = f(\mathbf{x}_d)$, where $f : \mathbb{R}^n \rightarrow \mathbb{R}^n$ is a locally lipschitz vector field, the dynamics in (1) can be linearly parametrized as follows

$$V_m(\mathbf{x}, \dot{\mathbf{x}})f(\mathbf{x}_d) + G(\mathbf{x}) + F(\dot{\mathbf{x}}) + M(\mathbf{x})\nabla f(\mathbf{x}_d)f(\mathbf{x}_d) = Y(\mathbf{x}, \dot{\mathbf{x}}, \mathbf{x}_d)\boldsymbol{\theta}, \quad (2)$$

where $Y(\mathbf{x}, \dot{\mathbf{x}}, \mathbf{x}_d) \in \mathbb{R}^{n \times n_{\boldsymbol{\theta}}}$ is a *regressor* matrix containing known and measured quantities, and $\boldsymbol{\theta} \in \mathbb{R}^{n_{\boldsymbol{\theta}}}$ is the corresponding vector of the constant unknown parameters.

Next, we present the design of a generalized control $\boldsymbol{\tau}$ that stabilizes the dynamics in (1) and is subsequently used in determining the power demand.

Theorem 1. *Consider the generalized vehicle dynamics in (1), together with a differentiable reference trajectory generated by the stable dynamics $\dot{\mathbf{x}}_d = f(\mathbf{x}_d)$. Let*

$$\boldsymbol{\eta}(t) \triangleq \dot{\mathbf{x}}(t) - \dot{\mathbf{x}}_d(t)$$

be the associated speed tracking error. Given positive real numbers k_1, γ_1 , the closed loop speed tracking error dynamics is globally asymptotically stable (GAS) under the control law

$$\boldsymbol{\tau}(t) = -k_1 \boldsymbol{\eta}(t) - \gamma_1 Y(t) \int_0^t Y(\nu)^\top \boldsymbol{\eta}(\nu) d\nu, \quad (3)$$

where $Y(t)$ is given in (2).

Proof. Consider the open-loop error dynamics

$$M(\mathbf{x})\dot{\boldsymbol{\eta}} = \boldsymbol{\tau} - V_m(\mathbf{x}, \dot{\mathbf{x}})\boldsymbol{\eta} - Y\boldsymbol{\theta} \quad (4)$$

substituting the designed control law in (3), the following closed-loop dynamics is obtained

$$M(\mathbf{x})\dot{\boldsymbol{\eta}} = -k_1\boldsymbol{\eta} - V_m(\mathbf{x}, \dot{\mathbf{x}})\boldsymbol{\eta} - Y\tilde{\boldsymbol{\theta}},$$

where

$$\begin{aligned} \tilde{\boldsymbol{\theta}} &= \boldsymbol{\theta} - \hat{\boldsymbol{\theta}}(t), \\ &= \boldsymbol{\theta} - \gamma_1 Y(t) \int_0^t Y(\nu)^\top \boldsymbol{\eta}(\nu) d\nu, \end{aligned}$$

is the parameter estimation error.

Consider the Lyapunov candidate function

$$V = \frac{1}{2} \boldsymbol{\eta}^\top M \boldsymbol{\eta} + \frac{1}{2\gamma_1} \tilde{\boldsymbol{\theta}}^\top \tilde{\boldsymbol{\theta}},$$

taking the first time derivative along the variables and making use of the skew-symmetric property and substituting the control law in (3) yields,

$$\dot{V} = -k_1 \|\boldsymbol{\eta}\|^2,$$

since \dot{V} is negative semi-definite and $V > 0$. Thus, $V \in \mathbb{L}_\infty$, which implies $\boldsymbol{\eta} \in \mathbb{L}_\infty$, since it is assumed that the reference speed $\dot{\mathbf{x}}_d \in \mathbb{L}_\infty$, it implies that $\dot{\mathbf{x}} \in \mathbb{L}_\infty$. Integrating \dot{V} yields,

$$V(\infty) - V(0) = -k_1 \int_0^\infty \|\boldsymbol{\eta}(t)\|^2 dt,$$

It follows that $\boldsymbol{\eta} \in \mathbb{L}_2$. Also $\boldsymbol{\eta}$ is uniformly continuous. Thus, invoking Barbalat's lemma [29] it follows that $\lim_{t \rightarrow \infty} \boldsymbol{\eta}(t) = \mathbf{0}$. \square

Remark 1. The resulting generalized power demand that needs to be tracked by the engine ($p_e \in \mathbb{R}$) and the battery ($p_b \in \mathbb{R}$) is given as $p_e + p_b = p_d$, where

$$p_d = -\dot{\mathbf{x}}^\top \left(k_1 \boldsymbol{\eta}(t) + \gamma_1 Y(t) \int_0^t Y(\nu)^\top \boldsymbol{\eta}(\nu) d\nu \right). \quad (5)$$

Fig. 3 shows the derived power demand given the speed profile for road vehicles (hybrid electric cars), surface vehicles (dynamically positioned ships), and aerial vehicles (hybrid electric aircraft).

We make the following remarks concerning special cases of the generalized vehicle dynamics in (1).

Remark 2 (Hybrid road vehicles). *The longitudinal vehicle dynamics [30] of hybrid road vehicles is of the form in (1) with*

$$\begin{aligned} M(x) &= m, & V_m(x, \dot{x}) &= 0, \\ G(x) &= \mu_r mg \cos(\phi), & F(\dot{x}) &= 0.5 \rho A C_d \dot{x}^2, \end{aligned}$$

where $\dot{x}(t) \in \mathbb{R}$ is the vehicle speed [in m/s], $\tau(t) \in \mathbb{R}$ is the effective wheel torque [in $N\cdot m$], $m \in \mathbb{R}_+$ is the mass of the vehicle [in kg], $\rho_d \in \mathbb{R}_+$ is density of air [in $Kg \cdot m^{-2}$], $C_d \in \mathbb{R}_+$ is the aerodynamic drag coefficient [no units], $A \in \mathbb{R}_+$ is the frontal area of the car [in m^2], $\mu_r \in \mathbb{R}_+$ is the coefficient of rolling resistance [no units], $g = 9.87 m/s^2$ is the acceleration due to gravity, $\phi \in \mathbb{R}_+$ is the road gradient (assumed to be constant), and R is the effective wheel radius in [m]. The road vehicle dynamics can be linearly parameterized as

$$Y = \begin{bmatrix} \dot{x}^2 \\ \ddot{x}_d^\top \\ 1 \end{bmatrix}^\top, \quad \boldsymbol{\theta} = \begin{bmatrix} 0.5 \rho A C_d \\ m \\ \mu_r mg \cos(\phi) \end{bmatrix} \in \mathbb{R}^3.$$

Remark 3 (Hybrid surface vehicles). *For hybrid ships and other thruster-driven hybrid surface vehicles [27], [31], the dynamics satisfy (1) with $M(\mathbf{x}) = R \bar{M} R^\top$, $V_m(\mathbf{x}, \dot{\mathbf{x}}) = R \bar{M} \dot{R}^\top$, $F(\dot{\mathbf{x}}) = R D R^\top \dot{\mathbf{x}}$ and $G(\mathbf{x}) = R K \mathbf{x}$, where*

$$\begin{aligned} R &= \begin{bmatrix} \cos(\psi) & -\sin(\psi) & 0 \\ \sin(\psi) & \cos(\psi) & 0 \\ 0 & 0 & 1 \end{bmatrix}, \\ \bar{M} &= \begin{bmatrix} m_{11} & 0 & 0 \\ 0 & m_{22} & m_{23} \\ 0 & m_{23} & m_{33} \end{bmatrix}, D = \begin{bmatrix} d_{11} & 0 & 0 \\ 0 & d_{22} & d_{23} \\ 0 & d_{23} & d_{33} \end{bmatrix}, \end{aligned}$$

and $K \in \mathbb{R}^{3 \times 3}$ is a diagonal matrix accounting for the mooring forces. R represents the rotation between the Earth and body-fixed coordinate frames, $M \in \mathbb{R}^{3 \times 3}$ denotes the positive-definite and symmetric constant mass-inertia matrix, $D \in \mathbb{R}^{3 \times 3}$ denotes the constant damping matrix. $\mathbf{x} \triangleq [x, y, \psi]^\top$ is the state vector consisting of the translational positions and the yaw angle. For the surface vehicles control input $\boldsymbol{\tau} \in \mathbb{R}^3$ denotes the control force/ control torque required to drive the propeller. The dynamics can be linearly parameterized as [27]

$$\begin{aligned} Y(\mathbf{x}, \dot{\mathbf{x}}, \ddot{\mathbf{x}}) &\in \mathbb{R}^{3 \times 9}, \\ \boldsymbol{\theta} &= [m_{11}; m_{22}; m_{23}; m_{33}; d_{11}; d_{22}; d_{23}; d_{32}; d_3] \in \mathbb{R}^9 \end{aligned}$$

Remark 4 (Hybrid aerial Vehicles). *For aerial vehicles such as hybrid electric aircraft, the longitudinal dynamical model is of the form in (1) with [32]*

$$\begin{aligned} M(x) &= m_a, & V_m(x, \dot{x}) &= 0, \\ G(x) &= m_a g \sin(\phi_a), & F(\dot{x}) &= 0.5 \rho_a S C_d \dot{x}^2, \end{aligned}$$

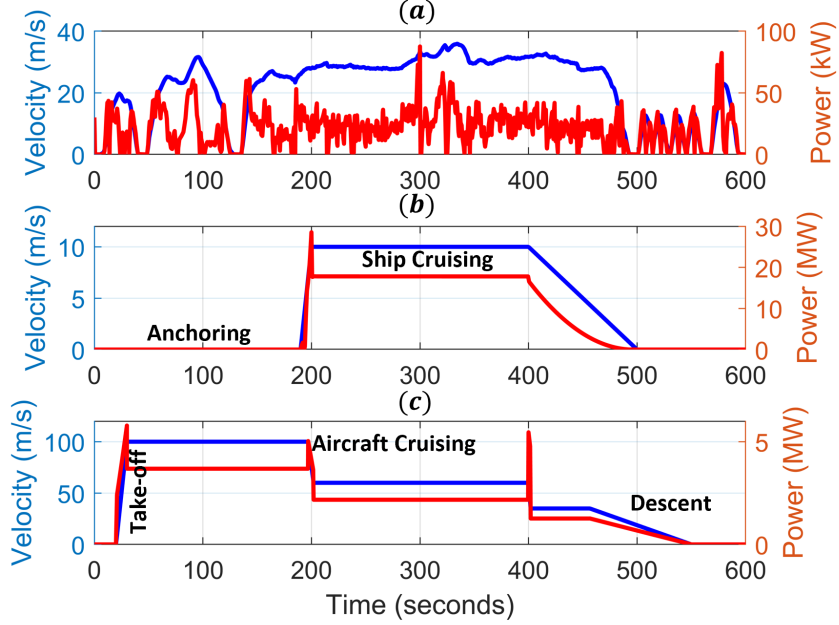


Figure 3: (a) Velocity and power required to track the velocity performance for the hybrid road vehicles, (b) Velocity and power required to track the velocity performance for the hybrid surface vehicles, (c) Velocity and power required to track the velocity performance for the hybrid aerial vehicles.

where $\dot{x}(t) \in \mathbb{R}$ is the aircraft longitudinal velocity [in m/s], $\tau(t) \in \mathbb{R}$ is the effective thrust [in N-m], $m_a \in \mathbb{R}_+$ is the mass of the aircraft [in kg], $\rho_a \in \mathbb{R}_+$ is density of air [in $\text{Kg}\cdot\text{m}^{-2}$], $C_d \in \mathbb{R}_+$ is the aerodynamic drag coefficient [no units], $S \in \mathbb{R}_+$ is the wing area of the aircraft [in m^2], $g = 9.87\text{m}/\text{s}^2$ is the acceleration due to gravity, $\phi_a \in \mathbb{R}_+$ is the aircraft path angle [in degree]. The road vehicle dynamics can be linearly parameterized as

$$Y = \begin{bmatrix} \dot{x}^2 \\ \ddot{x}_d \\ 1 \end{bmatrix}^\top, \theta = \begin{bmatrix} 0.5\rho_a C_d S \\ m_a \\ m_a g \sin(\phi_a) \end{bmatrix} \in \mathbb{R}^3$$

Next, we present the modeling of the energy storage system.

5 Energy Storage System Modeling

The Energy Storage System (ESS) constitutes a single or multiple hybrid energy storage elements. This might include a collection of flywheels, or supercapacitors. The dynamics of the ESS used in this work and the battery current

calculations are based on [33, 34]. The relationship between the ESS power injected p_b and the SoC is given as follows:

$$q(t) = q_0 - \frac{1}{Q_T v_b} \int_0^t p_b(\nu) d\nu, \quad (6)$$

where $Q_T \in \mathbb{R}_+$ is the total capacity of the battery in Ahr, $v_b \in \mathbb{R}_+$ denotes the battery voltage, which is algebraically expressed as

$$v_b = v_{oc}(q) - r_b i_b, \quad (7)$$

where $v_{oc}(q)$ is the open-circuit voltage which is a function of the state of charge. The relation between v_{oc} and SoC can be approximated using various functions ranging from lower to higher orders with the linear approximation being the fundamental one given as $v_{oc} = c_1 q + c_2$, where c_1, c_2 are constants [35]. r_b is the internal resistance of the battery and $i_b \in \mathbb{R}$ is the battery current, $q_0 \in [0, 1]$ is the initial SoC of the battery. Although the SoC dynamics above does not explicitly capture the physical restriction $q(t) \in [0, 1]$ for all $t \in \mathbb{R}_+$, we impose this explicit constraint in the underlying optimization problem of the proposed energy management strategy. As a result, it is ignored in the dynamics without loosing fidelity. The SoC dynamics in (6) is discretized, with a sampling time $T_s \in \mathbb{R}_+$, to obtain the following discrete dynamics:

$$\sum_{k=0}^N p_{b_k} = \frac{Q_T v_b}{T_s} (q_0 - q_N), \quad (8)$$

where q_N is the SoC at the time instant $NT_s \in \mathbb{R}_+$, and N is the number of discrete time samples in the prediction horizon.

The battery degradation model is based on the Arrhenius equation and uses the *Ah*-throughput $\int_0^t |i_b(\nu)| d\nu$ as a metric to evaluate the battery state of health (SoH), where $i_b(t) \in \mathbb{R}$ is the current drawn from the battery (positive in the discharge direction and vice-versa). The *capacity loss* is given as [36]:

$$Q_L(t) = e^{\frac{-\zeta_2 + T C_r}{RT}} \int_0^t |i_b(\nu)|^{\frac{1}{2}} d\nu, \quad (9)$$

where $T \in \mathbb{R}_+$ is the baseline temperature (in Kelvin) of the battery where it is most efficient and $C_r \in \mathbb{R}_+$ is the C-rate of the battery. The capacity loss (%) is given as follows:

$$\Delta Q\% = \frac{Q_T - Q_L(t)}{Q_T} \times 100,$$

where Q_L is the *capacity loss* of the ESS in ampere-hour. ΔQ only captures the *capacity loss* during the ESS operation.

We have presented the model development required and next we present the proposed energy management development.

6 Proposed Energy Management Method

The MPME scheme is given in the form of the optimization problem:

$$\begin{aligned}
\text{Minimize}_{p_{e_k}, p_{b_k}, q_k} \quad & \sum_{k=1}^h \left(\frac{\alpha}{2} (p_{e_k} + p_{b_k} - \hat{p}_{d_k})^2 + C_e(p_{e_k}) + C_b(p_{b_k}) \right) \\
\text{Subject to:} \quad & \underline{p}_e \preceq p_{e_k} \preceq \bar{p}_e, \quad \forall k = 1, 2, \dots, h, \\
& \underline{p}_b \preceq p_{b_k} \preceq \bar{p}_b, \quad \forall k = 1, 2, \dots, h, \\
& \underline{q} \preceq q_k \preceq \bar{q}, \quad \forall k = 1, 2, \dots, h, \\
& |p_{e_k} - p_{e_{k-1}}| \preceq r_e, \quad \forall k = 1, 2, \dots, h, \\
& |p_{b_k} - p_{b_{k-1}}| \preceq r_b, \quad \forall k = 1, 2, \dots, h, \\
& \sum_{k=1}^h p_{b_k} = \frac{Q_T v_b}{T_s} (q_0 - q_h),
\end{aligned} \tag{10}$$

where $[p_{e_1}, p_{e_2}, \dots, p_{e_h}]^\top \in \mathbb{R}^h$ is the engine power profile over a prediction horizon of length h , $[p_{b_1}, p_{b_2}, \dots, p_{b_h}]^\top \in \mathbb{R}^h$ is the battery power profile over a prediction horizon of length h , $[\hat{p}_{d_1}, \hat{p}_{d_2}, \dots, \hat{p}_{d_h}]^\top \in \mathbb{R}^h$ is the power forecast over the horizon of the length h assumed to be held constant for the length of the horizon, q_h is the SoC at the end of each horizon, $\alpha \in \mathbb{R}_+$ is the weighting associated with the power tracking objective. $C_e : \mathbb{R}^h \rightarrow \mathbb{R}_+$ is the cost function associated with the engine efficiency. $C_b : \mathbb{R}^h \rightarrow \mathbb{R}_+$ is the cost function associated with the battery degradation and health. The constraint set is a *polytope* comprised of an affine equality constraints and an affine inequality constraints. For the ease of exposition, we group the respective engine, and battery constraints as $\mathcal{P}_e, \mathcal{P}_b \subset \mathbb{R}^h$ representing individual constraint sets for each of the engine and the battery capturing their ramp-rate limitations and box constraints and relevant system dynamic constraints. The goal here is to split the optimization problem in (10) into two local optimization problems, one each for the engine and the battery. First, we write (10) as:

$$\begin{aligned}
\text{Minimize}_{y_{e_k}, y_{b_k}, p_{e_k}, p_{b_k}} \quad & \sum_{k=1}^h \left(\frac{\alpha}{2} (y_{e_k} + y_{b_k} - \hat{p}_{d_k})^2 + C_e(p_{e_k}) + C_b(p_{b_k}) \right) \\
\text{Subject to:} \quad & p_{e_k} = y_{e_k}, \quad \forall k = 1, 2, \dots, h, \\
& p_{b_k} = y_{b_k}, \quad \forall k = 1, 2, \dots, h, \\
& p_{e_k} \in \mathcal{P}_e, \quad \forall k = 1, 2, \dots, h, \\
& p_{b_k} \in \mathcal{P}_b, \quad \forall k = 1, 2, \dots, h,
\end{aligned} \tag{11}$$

where $y_{e_k}, y_{b_k} \in \mathbb{R}$ are the dummy variables introduced to split the problem. The optimization problem in (11) is written more compactly as

$$\begin{aligned} \text{Minimize: } & \frac{\alpha}{2} \|\mathbf{y}_e + \mathbf{y}_b - \hat{\mathbf{p}}_d\|_2^2 + C_e(\mathbf{p}_e) + C_b(\mathbf{p}_b) \\ \text{Subject to: } & \mathbf{p}_e = \mathbf{y}_e, \mathbf{p}_b = \mathbf{y}_b, \\ & \mathbf{p}_e \in \mathcal{P}_e, \mathbf{p}_b \in \mathcal{P}_b, \end{aligned} \quad (12)$$

where $\mathbf{y}_e \triangleq [y_{e_1}, y_{e_2}, \dots, y_{e_h}]^\top \in \mathbb{R}^h$, $\mathbf{y}_b \triangleq [y_{b_1}, y_{b_2}, \dots, y_{b_h}]^\top \in \mathbb{R}^h$, $\sum_{k=1}^h C_e(p_{e_k}) \triangleq C_e(\mathbf{p}_e)$ and $\sum_{k=1}^h C_b(p_{b_k}) \triangleq C_b(\mathbf{p}_b)$. for a given parameter $\rho > 0$, the augmented Lagrangian for the optimization problem in (12) is given as [37]:

$$\begin{aligned} \mathcal{L}_\rho(\mathbf{y}_e, \mathbf{y}_b, \mathbf{p}_e, \mathbf{p}_b, \boldsymbol{\lambda}_e, \boldsymbol{\lambda}_b) = & \frac{\alpha}{2} \|\mathbf{y}_e + \mathbf{y}_b - \hat{\mathbf{p}}_d\|_2^2 + C_e(\mathbf{p}_e) \\ & + C_b(\mathbf{p}_b) + \boldsymbol{\lambda}_e^\top (\mathbf{p}_e - \mathbf{y}_e) + \boldsymbol{\lambda}_b^\top (\mathbf{p}_b - \mathbf{y}_b) \\ & + \frac{\rho}{2} \|\mathbf{p}_e - \mathbf{y}_e\|_2^2 + \frac{\rho}{2} \|\mathbf{p}_b - \mathbf{y}_b\|_2^2 + \mathcal{I}_{\mathcal{P}_e} + \mathcal{I}_{\mathcal{P}_b}, \end{aligned}$$

where $\mathcal{I}_{\mathcal{P}_e}$ and $\mathcal{I}_{\mathcal{P}_b}$ are the indicator functions for the inclusion constraints $\mathbf{p}_e \in \mathcal{P}_e$ and $\mathbf{p}_b \in \mathcal{P}_b$ respectively. Equivalently, the Lagrangian in the scaled form is given as [37]

$$\begin{aligned} \mathcal{L}_\rho(\mathbf{y}_e, \mathbf{y}_b, \mathbf{p}_e, \mathbf{p}_b, \mathbf{u}_e, \mathbf{u}_b) = & \frac{\alpha}{2} \|\mathbf{y}_e + \mathbf{y}_b - \hat{\mathbf{p}}_d\|_2^2 + C_e(\mathbf{p}_e) \\ & + C_b(\mathbf{p}_b) + \frac{\rho}{2} \|\mathbf{p}_e - \mathbf{y}_e + \mathbf{u}_e\|_2^2 \\ & + \frac{\rho}{2} \|\mathbf{p}_b - \mathbf{y}_b + \mathbf{u}_b\|_2^2 - \frac{\rho}{2} \|\mathbf{u}_e\|_2^2 - \frac{\rho}{2} \|\mathbf{u}_b\|_2^2 + \mathcal{I}_{\mathcal{P}_e} + \mathcal{I}_{\mathcal{P}_b}, \end{aligned}$$

where $\mathbf{u}_e \triangleq \frac{1}{\rho} \boldsymbol{\lambda}_e$ and $\mathbf{u}_b \triangleq \frac{1}{\rho} \boldsymbol{\lambda}_b$.

Consequently, following the Gauss-Seidel alternating minimization, one obtains the following successive iterative scheme [37]:

$$\mathbf{y}_e^{t+1} = \arg \min_{\mathbf{y}_e} \left\{ \frac{\alpha}{2} \|\mathbf{y}_e + \mathbf{y}_b - \hat{\mathbf{p}}_d\|_2^2 + \frac{\rho}{2} \|\mathbf{p}_e^t - \mathbf{y}_e + \mathbf{u}_e^t\|_2^2 \right\}, \quad (13a)$$

$$\mathbf{y}_b^{t+1} = \arg \min_{\mathbf{y}_b} \left\{ \frac{\alpha}{2} \|\mathbf{y}_e + \mathbf{y}_b - \hat{\mathbf{p}}_d\|_2^2 + \frac{\rho}{2} \|\mathbf{p}_b^t - \mathbf{y}_b + \mathbf{u}_b^t\|_2^2 \right\}, \quad (13b)$$

$$\mathbf{p}_e^{t+1} = \arg \min_{\mathbf{p}_e \in \mathcal{P}_e} \left\{ C_e(\mathbf{p}_e) + \frac{\rho}{2} \|\mathbf{p}_e - \mathbf{y}_e^{t+1} + \mathbf{u}_e^t\|_2^2 \right\}, \quad (13c)$$

$$\mathbf{p}_b^{t+1} = \arg \min_{\mathbf{p}_b \in \mathcal{P}_b} \left\{ C_b(\mathbf{p}_b) + \frac{\rho}{2} \|\mathbf{p}_b - \mathbf{y}_b^{t+1} + \mathbf{u}_b^t\|_2^2 \right\}, \quad (13d)$$

$$\mathbf{u}_e^{t+1} = \mathbf{u}_e^t + \mathbf{p}_e^{t+1} - \mathbf{y}_e^{t+1}, \quad (13e)$$

$$\mathbf{u}_b^{t+1} = \mathbf{u}_b^t + \mathbf{p}_b^{t+1} - \mathbf{y}_b^{t+1}. \quad (13f)$$

The convergence of iterations in (13) is a well-studied topic and is available in [37]. The optimization problems in (13a) and (13b) are unconstrained quadratic programs and a closed-form solution can be readily obtained.

Theorem 2. *The optimization steps in (13a) and (13b) are equivalent to:*

$$\begin{aligned}\mathbf{y}_e^{t+1} &= \mathbf{p}_e^t + \mathbf{u}_e^t + \mathbf{a}^t, \\ \mathbf{y}_b^{t+1} &= \mathbf{p}_b^t + \mathbf{u}_b^t + \mathbf{a}^t,\end{aligned}$$

where

$$\mathbf{a}^t = \frac{\alpha}{2\alpha + \rho} \left(\hat{\mathbf{p}}_d - (\mathbf{p}_e^t + \mathbf{p}_b^t + \mathbf{u}_e^t + \mathbf{u}_b^t) \right).$$

Proof. The first order optimality conditions for (13a) and (13b) are:

$$\alpha \left(\mathbf{y}_e^* + \mathbf{y}_b^* - \hat{\mathbf{p}}_d \right) - \rho \left(\mathbf{p}_e^t - \mathbf{y}_e^* + \mathbf{u}_e^t \right) = 0, \quad (14a)$$

$$\alpha \left(\mathbf{y}_e^* + \mathbf{y}_b^* - \hat{\mathbf{p}}_d \right) - \rho \left(\mathbf{p}_b^t - \mathbf{y}_b^* + \mathbf{u}_b^t \right) = 0. \quad (14b)$$

Rewriting the above equation in the matrix form combining both (14a) and (14b) yields:

$$\left(\frac{\alpha}{\rho} \begin{bmatrix} I_h \\ I_h \end{bmatrix} \begin{bmatrix} I_h \\ I_h \end{bmatrix}^\top + \begin{bmatrix} I_h \\ I_h \end{bmatrix} \right) \begin{bmatrix} \mathbf{y}_e^* \\ \mathbf{y}_b^* \end{bmatrix} = \frac{\alpha}{\rho} \begin{bmatrix} \hat{\mathbf{p}}_d \\ \hat{\mathbf{p}}_d \end{bmatrix} + \begin{bmatrix} \mathbf{p}_e^t \\ \mathbf{p}_b^t \end{bmatrix} + \begin{bmatrix} \mathbf{u}_e^t \\ \mathbf{u}_b^t \end{bmatrix}. \quad (15)$$

Using the matrix inversion lemma, it follows that

$$\begin{aligned}\mathbf{y}_e^* &= \mathbf{p}_e^t + \mathbf{u}_e^t + \frac{\alpha}{2\alpha + \rho} \left(\hat{\mathbf{p}}_d - (\mathbf{p}_e^t + \mathbf{p}_b^t + \mathbf{u}_e^t + \mathbf{u}_b^t) \right) \\ \mathbf{y}_b^* &= \mathbf{p}_b^t + \mathbf{u}_b^t + \underbrace{\frac{\alpha}{2\alpha + \rho} \left(\hat{\mathbf{p}}_d - (\mathbf{p}_e^t + \mathbf{p}_b^t + \mathbf{u}_e^t + \mathbf{u}_b^t) \right)}_{\triangleq \mathbf{a}^t}\end{aligned}$$

□

From Theorem 2, it is seen that \mathbf{a}^t acts as an aggregator or a communicator between the engine and the battery nodes updating the dual variable. Thus each node implements the following successive optimization problems at each iteration:

$$\mathbf{y}_e^{t+1} = \mathbf{p}_e^t + \mathbf{u}_e^t + \mathbf{a}^t, \quad (16a)$$

$$\mathbf{y}_b^{t+1} = \mathbf{p}_b^t + \mathbf{u}_b^t + \mathbf{a}^t, \quad (16b)$$

$$\mathbf{p}_e^{t+1} = \arg \min_{\mathbf{p}_e \in \mathcal{P}_e} \left\{ C_e(\mathbf{p}_e) + \frac{\rho}{2} \|\mathbf{p}_e - \mathbf{y}_e^{t+1} + \mathbf{u}_e^t\|_2^2 \right\}, \quad (16c)$$

$$\mathbf{p}_b^{t+1} = \arg \min_{\mathbf{p}_b \in \mathcal{P}_b} \left\{ C_b(\mathbf{p}_b) + \frac{\rho}{2} \|\mathbf{p}_b - \mathbf{y}_b^{t+1} + \mathbf{u}_b^t\|_2^2 \right\}, \quad (16d)$$

$$\mathbf{u}_e^{t+1} = \mathbf{u}_e^t + \mathbf{p}_e^{t+1} - \mathbf{y}_e^{t+1}, \quad (16e)$$

$$\mathbf{u}_b^{t+1} = \mathbf{u}_b^t + \mathbf{p}_b^{t+1} - \mathbf{y}_b^{t+1}. \quad (16f)$$

Proposition 1. *The iterative scheme in (16a-16f) is equivalent to the dynamic updates:*

$$\begin{aligned}\mathbf{p}_e^{t+1} &= \arg \min_{\mathbf{p}_e \in \mathcal{P}_e} \left\{ C_e(\mathbf{p}_e) + \frac{\rho}{2} \|\mathbf{p}_e - \mathbf{p}_e^t - \mathbf{a}^t\|_2^2 \right\}, \\ \mathbf{z}_e^{t+1} &= 2\mathbf{p}_e^{t+1} - \mathbf{p}_e^t - \mathbf{a}^t,\end{aligned}\quad (17a)$$

$$\begin{aligned}\mathbf{p}_b^{t+1} &= \arg \min_{\mathbf{p}_b \in \mathcal{P}_b} \left\{ C_b(\mathbf{p}_b) + \frac{\rho}{2} \|\mathbf{p}_b - \mathbf{p}_b^t - \mathbf{a}^t\|_2^2 \right\}, \\ \mathbf{z}_b^{t+1} &= 2\mathbf{p}_b^{t+1} - \mathbf{p}_b^t - \mathbf{a}^t,\end{aligned}\quad (17b)$$

$$\mathbf{a}^t = \frac{\alpha}{2\alpha + \rho} (\hat{\mathbf{p}}_d - \mathbf{z}_e^t - \mathbf{z}_b^t), \quad (17c)$$

where $\mathbf{z}^t \triangleq \mathbf{p}^t + \mathbf{u}^t$.

Remark 5. *Proposition 1 expresses the iterative scheme in (16a-16f) to distributed dynamic updates where (17a) and (17b) are parallel operations for the engine and battery nodes optimization respectively, and (17c) is the aggregator that couples them via the dual updates. This is shown schematically in Fig 4.*

Proof. Substituting (16a) in (16e) and (16b) in (16f) we get,

$$\begin{aligned}\mathbf{z}_e^{t+1} &= \mathbf{p}_e^{t+1} + \mathbf{u}_e^t + \mathbf{p}_e^{t+1} - \mathbf{p}_e^t - \mathbf{u}_e^t - \mathbf{a}^t, \\ &= 2\mathbf{p}_e^{t+1} - \mathbf{p}_e^t - \mathbf{a}^t.\end{aligned}$$

$$\begin{aligned}\mathbf{z}_b^{t+1} &= \mathbf{p}_b^{t+1} + \mathbf{u}_b^t + \mathbf{p}_b^{t+1} - \mathbf{p}_b^t - \mathbf{u}_b^t - \mathbf{a}^t, \\ &= 2\mathbf{p}_b^{t+1} - \mathbf{p}_b^t - \mathbf{a}^t.\end{aligned}$$

substituting (16a) in (16c) and (16b) in (16d) we get:

$$\begin{aligned}\mathbf{p}_e^{t+1} &= \arg \min_{\mathbf{p}_e \in \mathcal{P}_e} \left\{ C_e(\mathbf{p}_e) + \frac{\rho}{2} \|\mathbf{p}_e - \mathbf{p}_e^t - \mathbf{a}^t\|_2^2 \right\} \\ \mathbf{p}_b^{t+1} &= \arg \min_{\mathbf{p}_b \in \mathcal{P}_b} \left\{ C_b(\mathbf{p}_b) + \frac{\rho}{2} \|\mathbf{p}_b - \mathbf{p}_b^t - \mathbf{a}^t\|_2^2 \right\},\end{aligned}$$

thus completing the proof. \square

Next, the individual nodal level optimization problems are given, with explicitly specified choices for the functions C_e , C_b , and node-specific inclusion constraints for the respective nodes.

6.1 Optimization Problem at Engine Node

The optimization problem at the engine node is given as:

$$\begin{aligned}
 \text{Minimize}_{\mathbf{p}_e} \quad & \frac{\beta}{2} \|\mathbf{p}_e - \mathbf{p}_e^r\|_2^2 + \frac{\rho}{2} \|\mathbf{p}_e - \mathbf{p}_e^t - \mathbf{a}^t\|_2^2 \\
 \text{Subject to:} \quad & \underline{\mathbf{p}}_e \preceq \mathbf{p}_e \preceq \bar{\mathbf{p}}_e, \\
 & \begin{bmatrix} D \\ -D \end{bmatrix} \mathbf{p}_e \preceq r_e \mathbf{1},
 \end{aligned} \tag{18}$$

where

$$D \triangleq I_h - \begin{pmatrix} \mathbf{0}^\top & 0 \\ I_{h-1} & \mathbf{0} \end{pmatrix} \in \mathbb{R}^{h \times h},$$

is the point-wise difference operator through the prediction horizon, r_e is the ramp-rate limit of the engine pertaining to the engine torque limitation, \mathbf{p}_e^r is the most efficient operating point of the engine chosen based on the engine efficiency data, and $\bar{\mathbf{p}}_e$ and $\underline{\mathbf{p}}_e$ are the upper and lower limits on engine power respectively. Here, the choice $C_e(\mathbf{p}_e) = \frac{\beta}{2} \|\mathbf{p}_e - \mathbf{p}_e^r\|_2^2$ penalizes the deviation from the known efficient operation of the engine. The penalty factor β is a tuning parameter to weigh the relative importance of the engine efficiency cost against the algorithm convergence speed.

6.2 Optimization problem at Battery Node

The optimization problem at the battery node is given as:

$$\begin{aligned}
 \text{Minimize}_{\mathbf{p}_b, \mathbf{q}} \quad & \frac{\gamma}{2} \|\mathbf{p}_b\|_2^2 + \frac{\rho}{2} \|\mathbf{p}_b - \mathbf{p}_b^t - \mathbf{a}^t\|_2^2 \\
 \text{Subject to:} \quad & \sum_{k=1}^h \mathbf{p}_b = \kappa(\mathbf{q}_0 - \mathbf{q}_h), \\
 & \underline{\mathbf{p}}_b \preceq \mathbf{p}_b \preceq \bar{\mathbf{p}}_b, \\
 & \underline{\mathbf{q}} \preceq \mathbf{q} \preceq \bar{\mathbf{q}}, \\
 & \begin{bmatrix} D \\ -D \end{bmatrix} \mathbf{p}_b \preceq r_b \mathbf{1},
 \end{aligned} \tag{19}$$

where $C_b(\mathbf{p}_b) = \frac{\gamma}{2} \|\mathbf{p}_b\|_2^2$ is the cost function minimizing the battery power and γ is the penalty factor that is tuned to weight the importance of battery usage, q_0 is the initial state of charge measurement from the system. $\kappa = Q_T v_b / T_s$, $\bar{\mathbf{p}}_b$ and $\underline{\mathbf{p}}_b$ represent upper and lower limits on battery power respectively, \mathbf{q}_0 and \mathbf{q}_h represent the initial SoC and the SoC at the end for the length of the horizon, $\underline{\mathbf{q}}$ and $\bar{\mathbf{q}}$ represent the upper and lower SoC limitations. r_b represents the ramp-rate limitation of the battery.

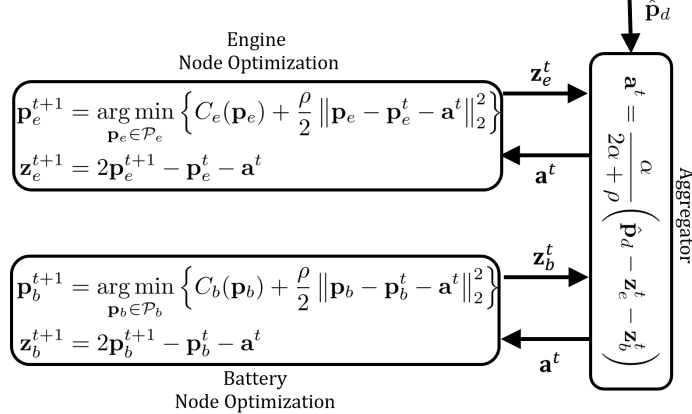


Figure 4: Distributed optimization implementation scheme

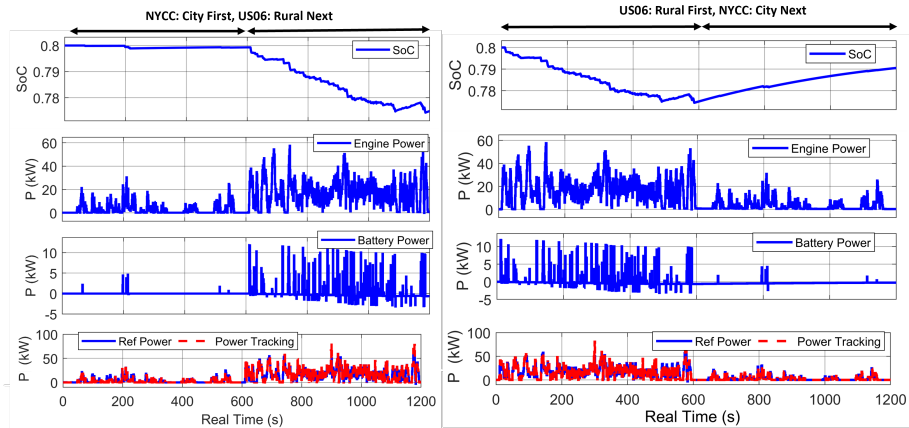


Figure 5: State of charge, engine optimal power, battery optimal power, and the power tracking for one simulation run for US06 drive-cycle and NYCC drive-cycle swapping the driving profiles.

7 Real-Time Numerical Simulation - Hybrid Electric Vehicle, dynamically positioned hybrid ship and hybrid electric aircraft

We present three real-time simulation test cases using hybrid electric vehicles (hybrid road vehicles), dynamically positioned ships (hybrid surface vehicles), and hybrid electric aircraft (hybrid aerial vehicles) to test the developed distributed algorithm. The real-time simulation setup consists of a Host PC connected to a real-time performance target machine (SPEEDGOAT in this case)

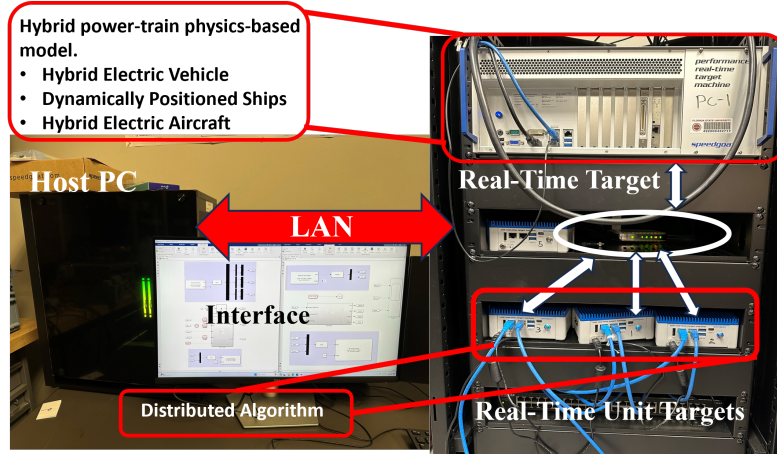


Figure 6: Real-time Setup

and three other smaller real-time unit target machines over a local area network (LAN) connection (1000 MBPS) receive/transmit link speed through a switch. Fig. 6 shows the setup in the lab. The longitudinal dynamics are implemented in the target machine and the distributed algorithm is deployed on the unit targets. The computational capabilities of the devices are provided in Table-1.

Table 1: Computational Info for RT-Setup

Device Name	CPU	RAM
Host PC	Intel Core i9 3.20GHz 24-core	64GB
Target	Intel Core 3.6GHz, 8-core	32GB
Unit Target-1	Intel Atom x5-E3940 1.6GHz 4-core	4GB

Table 2: Table Showing Rated Powers and Limits of the Engine and the Battery

Parameter	Value
Rated Engine Power	150hp or 112kW
Rated Battery Power	15kW
Desired Operating Engine Power	75kW
Engine Upper Power Limit	100kW
Battery Upper Power Limit	14kW
Battery Lower Power Limit	-14kW
State of Charge Lower Limit	0.5
State of Charge Upper Limit	0.8

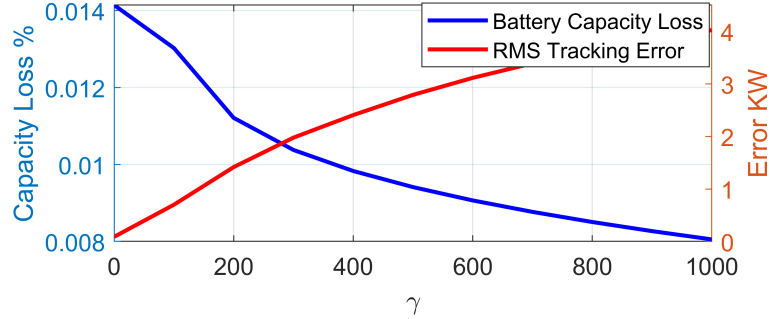


Figure 7: Figure shows the battery capacity loss versus the weight gamma and the power tracking error versus the gamma weight.

7.1 Hybrid Electric Vehicle

The proposed algorithm along with the developed model of a HEV is tested in a real-time MATLAB-Simulink environment. The optimization problems presented in (18) and (19) are used in the simulation process. The parameters for the HEV drive-line are chosen as $m = 1400\text{kg}$, $r = 0.2\text{m}$, $\rho_d = 1.225\text{Kg}\cdot\text{m}^{-2}$, $C_d = 0.35$, $A = 1.93\text{m}^2$, $\mu_{rr} = 0.03$. The optimization parameters which are fixed across the simulations are: $\alpha = 1000$, $\beta = 1$, $\rho = 0.1$, and $h = 5\text{seconds}$. The simulation is run at a fixed time-step of 1ms, with the optimization problem running every 1second. The power ratings and the power limits of the engine and the battery are given in Table 2.

Fig. 5 shows the high-level energy management. The absolute total power demand and the engine and battery combined tracked power in kW, the optimal engine power in kW, the optimal battery power in kW, and the state of charge of the battery are demonstrated for a real data using the US06 (rural), and New York city cycle (NYCC: city) drive-cycle data. Two scenarios are simulated 1) city first, rural next and 2) rural first, city next. It can be seen that the battery is used conservatively and is only deployed when there is a high power demand scenario. Another observation regarding the SoC of the battery and its charging and discharging pattern should also be observed. During the normal power operation, the battery can be seen charging for rural first and city next. Whenever, the demand is not high, the controller charges the battery to be around the SoC of 0.8 (which is the upper limit).

Next, the impact of the battery weight γ on the battery operation is studied. The value of γ is tuned from $[0 - 1000]$ while keeping the other weights constant. Fig. 7 presents the relationship between γ and the battery capacity loss %. As the value of γ increases, the battery capacity loss % decreases indicating less battery usage. However, it can also be seen from the plot that the power tracking error in kW increases. Thus, the trade-off between the battery health and tracking error is inferred from the results.

Finally, the effect of the weight γ is tested using three real drive-cycle data

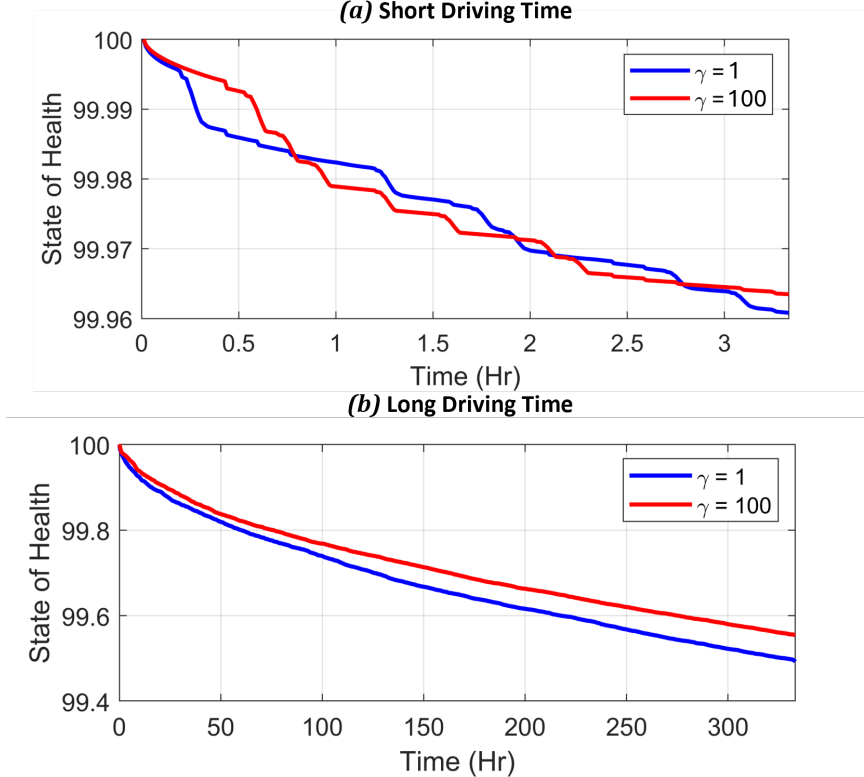


Figure 8: State of Health deterioration for different values of γ for a hybrid electric vehicle, (a) for a short driving duration, (b) for a long driving duration.

sets (US06, NYCC, SC03). The choice behind this selection is to incorporate both the highway (US06, SC03) and the city driving (NYCC) conditions. The drive cycles were randomized for every simulation run and around 2000 simulations were performed accumulating to the total driving time of around 360 hours. The aforementioned simulation was performed for different weights of γ (1 and 100). Fig. 8 shows the result of the above simulated scenarios. While, during the short drive time i.e. around 2-3 hours of driving, the effect of γ on battery health cannot be seen clearly. But it can be noticed that, as the driving time increases, even with different randomized drive-cycles, the effect of the weight γ begins to appear.

7.2 Dynamically Positioned Hybrid Ships

Next, we test the developed distributed algorithm to facilitate battery health-conscious power split for a dynamically positioned hybrid ship. To that extent, we design a velocity reference profile in such a way that the ship is initially

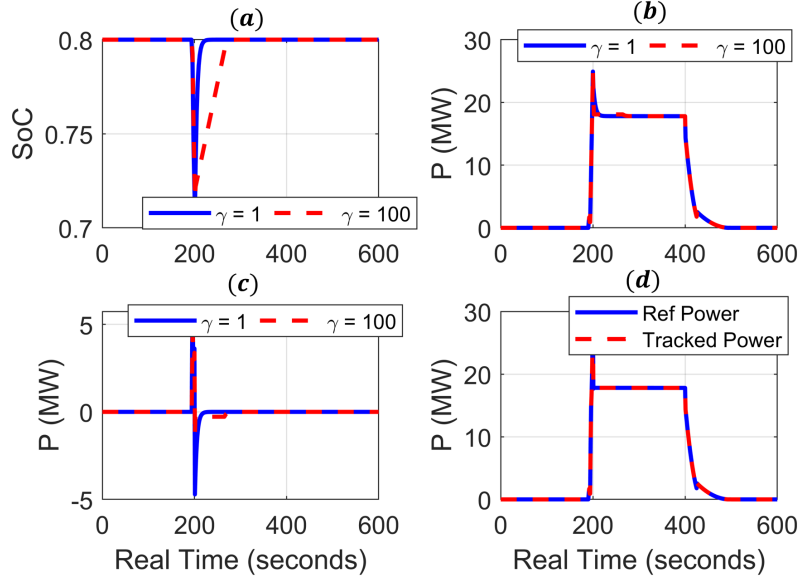


Figure 9: (a) State of charge, (b) engine power, (c) battery power and (d) power tracking for a dynamically positioned ship while anchoring, while ramping to cruising speed and de-ramping back to anchoring for $\gamma = 1$ and $\gamma = 100$.

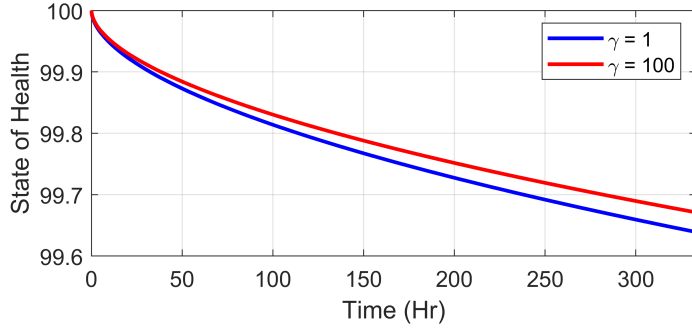


Figure 10: State of Health deterioration for different values of γ for a dynamically positioned ship.

anchored and then ramps up swiftly to the cruising speed (typically 10m/s or 19.4knots) and then de-ramps slowly back to anchoring position. The optimization parameters fixed across the simulations are $\alpha = 1000$, $\beta = 1$, $\rho = 0.1$, and $h = 5\text{seconds}$. The simulation is run at a fixed time-step of 1ms, with the optimization problem running every 1second. The mass of the ship is assumed to be around 1000ton. The rated engine power is 40MW, the rated battery power is 10MW, the state of charge upper and lower limits 0.8, and 0.5, ramp-rate of

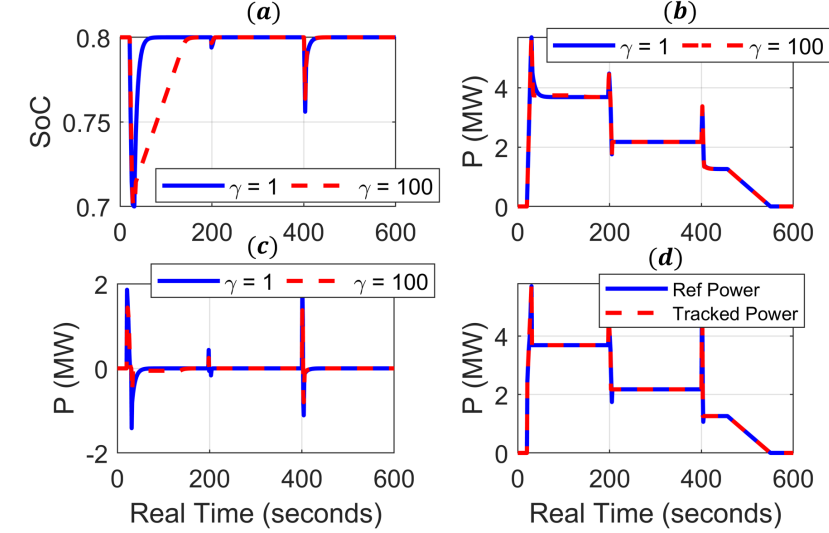


Figure 11: (a) State of charge, (b) engine power, (c) battery power, and (d) power tracking for a hybrid electric aircraft while taking off, cruising at an altitude, and while descending back for $\gamma = 1$, and $\gamma = 100$.

engine 10% of rated engine power, ramp-rate of the battery 90% of the rated battery power. Fig. 9 shows the state of charge, engine power, battery power, and the power tracking performance of the designed algorithm.

Fig. 10 shows the state of health of the battery for different values of the battery penalty weight γ . It can be seen that as the penalty of the battery is increased, more importance is given to mitigating the battery degradation.

7.3 Hybrid Electric Aircraft

Next, we test the developed distributed algorithm on a hybrid electric vehicle, the velocity profile is designed so that the take-off maneuver, followed by fixed altitude cruising action, followed by the descent action are considered. The parameters for the hybrid electric aircraft chosen based on [32] as $m_a = 42000\text{kg}$, $\rho_a = 1.225\text{Kg}\cdot\text{m}^{-2}$, $C_d = 0.03$, $S = 77.3\text{m}^2$. The power ratings considered for the engine and battery are 6MW, and 2MW. The ramping capacities are chosen as 10% of rated engine power, and 90% of the rated battery power. Fig. 11 shows the state of charge, engine power, and battery power for multiple values of the battery weights $\gamma = 1$, and $\gamma = 100$. The fixed optimization parameters α, β, h are similar to the ones used for HEV and DPS. To avoid redundancy, we do not explicitly present them.

The impact of the different battery penalty weights γ is shown in Fig. 12. It can be inferred that the power ratings of the engine, and the battery play a key role in determining the battery degradation. Moreover, the HEA power

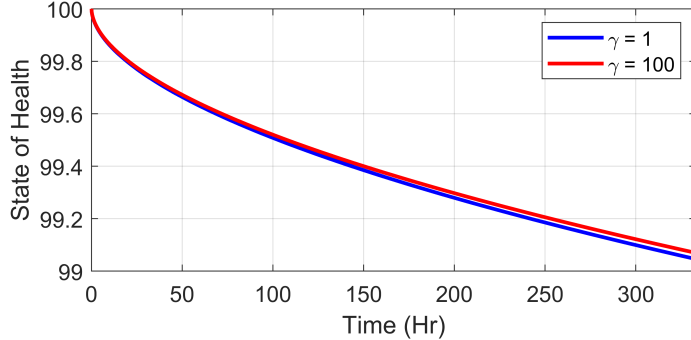


Figure 12: State of Health deterioration for different values of γ for a hybrid electric aircraft.

demand also plays an important role in determining battery degradation.

Overall, across multiple real-time numerical simulations on HEV, DPS, and HEA, the observation remains the same in terms of mitigating battery usage at the expense of more engine usage. The trade-off can be derived between efficient engine operation and conservative battery usage. Thus, the importance of the designed algorithm and the importance of the appropriate battery weighting to mitigate battery degradation has been effectively demonstrated.

8 Conclusion

We considered battery degradation in HEV and developed a corresponding health-heuristic-based model predictive energy management strategy that adaptively splits the power in a distributed framework. The choice of minimizing the battery power as a heuristic to mitigate the battery degradation is shown, through simulation by considering realistic drive cycle data from the U.S. EPA for hybrid electric vehicles and a simulation duration of 360 hours for hybrid electric vehicles, dynamically positioned hybrid ships, and hybrid electric aircraft to improve battery longevity while not sacrificing engine-efficient operation. The results presented demonstrate the operation of the designed algorithm and its effectiveness in mitigating battery degradation. Although the splitting problem was completely derived and results demonstrated via a more realistic simulation, as compared to related works in literature, the overall stability assessment with the designed algorithm relied on well-known stability properties of the MPC problem. The effect of the delays in the algorithm will be reported in the future extensions of this work.

References

- [1] C. C. Chan, “The state of the art of electric, hybrid, and fuel cell vehicles,” *Proceedings of the IEEE*, vol. 95, no. 4, pp. 704–718, 2007.
- [2] H. Banvait, S. Anwar, and Y. Chen, “A rule-based energy management strategy for plug-in hybrid electric vehicle (phev),” in *2009 American control conference*. IEEE, 2009, pp. 3938–3943.
- [3] H. Borhan, A. Vahidi, A. M. Phillips, M. L. Kuang, I. V. Kolmanovsky, and S. Di Cairano, “Mpc-based energy management of a power-split hybrid electric vehicle,” *IEEE Transactions on Control Systems Technology*, vol. 20, no. 3, pp. 593–603, 2011.
- [4] S. East and M. Cannon, “Energy management in plug-in hybrid electric vehicles: Convex optimization algorithms for model predictive control,” *IEEE Transactions on Control Systems Technology*, vol. 28, no. 6, pp. 2191–2203, 2019.
- [5] X. Hu, T. Liu, X. Qi, and M. Barth, “Reinforcement learning for hybrid and plug-in hybrid electric vehicle energy management: Recent advances and prospects,” *IEEE Industrial Electronics Magazine*, vol. 13, no. 3, pp. 16–25, 2019.
- [6] L. Xue, Y. Wang, P. Bogdan, N. Chang, and M. Pedram, “Reinforcement learning based power management for hybrid electric vehicles,” in *IEEE/ACM International Conference on Computer-Aided Design (ICCAD)*, IEEE, San Jose, CA, USA, 2014.
- [7] M. G. Vayá, G. Andersson, and S. Boyd, “Decentralized control of plug-in electric vehicles under driving uncertainty,” in *IEEE PES innovative smart grid technologies, Europe*. IEEE, 2014, pp. 1–6.
- [8] S. J. Moura, H. K. Fathy, D. S. Callaway, and J. L. Stein, “A stochastic optimal control approach for power management in plug-in hybrid electric vehicles,” *IEEE Transactions on control systems technology*, vol. 19, no. 3, pp. 545–555, 2010.
- [9] W. Golebiewski, K. Prajwowski, K. Danilecki, M. Lisowski, and K. F. Abramek, “Reducing the fuel consumption of an hybrid electric vehicle with the use of model predictive control-case study,” *IEEE Transactions on Vehicular Technology*, vol. 72, no. 9, pp. 11 458–11 468, 2023.
- [10] S. East and M. Cannon, “Scenario model predictive control for data-based energy management in plug-in hybrid electric vehicles,” *IEEE Transactions on Control Systems Technology*, vol. 30, no. 6, pp. 2522–2533, 2022.
- [11] D. Shen, D. Karbowski, and A. Rousseau, “Solving eco-driving problems using indirect collocation method and smooth representation,” in *2021 American Control Conference (ACC)*. IEEE, 2021, pp. 1631–1636.

- [12] C. Jia, W. Qiao, J. Cui, and L. Qu, “Adaptive model-predictive-control-based real-time energy management of fuel cell hybrid electric vehicles,” *IEEE Transactions on Power Electronics*, vol. 38, no. 2, pp. 2681–2694, 2022.
- [13] J. Kim, Y. Park, J. D. Fox, S. P. Boyd, and W. Dally, “Optimal operation of a plug-in hybrid vehicle with battery thermal and degradation model,” in *2020 American Control Conference (ACC)*. IEEE, 2020, pp. 3083–3090.
- [14] A. Khalatbarisoltani, M. Kandidayeni, L. Boulon, and X. Hu, “Comparison of decentralized admm optimization algorithms for power allocation in modular fuel cell vehicles,” *IEEE/ASME Transactions on Mechatronics*, vol. 27, no. 5, pp. 3297–3308, 2021.
- [15] X. Hu, C. Zou, X. Tang, T. Liu, and L. Hu, “Cost-optimal energy management of hybrid electric vehicles using fuel cell/battery health-aware predictive control,” *ieee transactions on power electronics*, vol. 35, no. 1, pp. 382–392, 2019.
- [16] A. Mehraban, E. Farjah, T. Ghambari, and L. Garbuio, “Integrated optimal energy management and sizing of hybrid battery/flywheel energy storage for electric vehicles,” *IEEE Transactions on Industrial Informatics*, 2023.
- [17] S. Li, P. Zhao, C. Gu, D. Huo, J. Li, and S. Cheng, “Linearizing battery degradation for health-aware vehicle energy management,” *IEEE Transactions on Power Systems*, 2022.
- [18] F. Ju, N. Murgovski, W. Zhuang, Q. Wang, and L. Wang, “Predictive cruise controller for electric vehicle to save energy and extend battery lifetime,” *IEEE Transactions on Vehicular Technology*, vol. 72, no. 1, pp. 469–482, 2022.
- [19] S. T. Miikka Jaurola, Anders Hedin and K. Huhtala, “Optimising design and power management in energy-efficient marine vessel power systems: a literature review,” *Journal of Marine Engineering & Technology*, vol. 18, no. 2, pp. 92–101, 2019. [Online]. Available: <https://doi.org/10.1080/20464177.2018.1505584>
- [20] I. Hazra, M. J. Weiner, R. Yang, A. Chatterjee, J. Southgate, K. M. Groth, and S. Azarm, “Prognostics and Health Management of Unmanned Surface Vessels: Past, Present, and Future,” *Journal of Computing and Information Science in Engineering*, vol. 24, no. 8, p. 080801, 06 2024. [Online]. Available: <https://doi.org/10.1115/1.4065483>
- [21] N. Planakis, G. Papalambrou, and N. Kyrtatos, “Integrated Load-Split Scheme for Hybrid Ship Propulsion Considering Transient Propeller Load and Environmental Disturbance,” *Journal of Dynamic Systems, Measurement, and Control*, vol. 143, no. 3, p. 031004, 10 2020. [Online]. Available: <https://doi.org/10.1115/1.4048588>

- [22] T. Q. Dinh, T. M. Bui, J. Marco, C. Watts, and J. I. Yoon, “Optimal energy management for hybrid electric dynamic positioning vessels,” *IFAC-PapersOnLine*, vol. 51, no. 29, pp. 98–103, 2018, 11th IFAC Conference on Control Applications in Marine Systems, Robotics, and Vehicles CAMS 2018. [Online]. Available: <https://www.sciencedirect.com/science/article/pii/S2405896318321657>
- [23] C. Bordin and O. Mo, “Including power management strategies and load profiles in the mathematical optimization of energy storage sizing for fuel consumption reduction in maritime vessels,” *Journal of Energy Storage*, vol. 23, pp. 425–441, 2019. [Online]. Available: <https://www.sciencedirect.com/science/article/pii/S2352152X18306790>
- [24] S. R. Hashemi, R. Esmaeeli, A. Nazari, H. Aliniagerdroudbari, M. Alhadri, W. Zakri, A. H. Mohammed, A. Mahajan, and S. Farhad, “A Fast Diagnosis Methodology for Typical Faults of a Lithium-Ion Battery in Electric and Hybrid Electric Aircraft,” *Journal of Electrochemical Energy Conversion and Storage*, vol. 17, no. 1, p. 011011, 10 2019. [Online]. Available: <https://doi.org/10.1115/1.4044956>
- [25] *Integrated Hybrid Engine Cycle Design and Power Management Optimization*, ser. Turbo Expo: Power for Land, Sea, and Air, vol. Volume 1: Aircraft Engine, 06 2023. [Online]. Available: <https://doi.org/10.1115/GT2023-103131>
- [26] V. G. Gkoutzamanis, M. D. Kavvalos, A. Srinivas, D. Mavroudi, G. Korbetis, K. G. Kyriyanidis, and A. I. Kalfas, “Conceptual Design and Energy Storage Positioning Aspects for a Hybrid-Electric Light Aircraft,” *Journal of Engineering for Gas Turbines and Power*, vol. 143, no. 9, p. 091019, 06 2021. [Online]. Available: <https://doi.org/10.1115/1.4050870>
- [27] W. E. Dixon, A. Behal, D. M. Dawson, and S. P. Nagarkatti, *Nonlinear control of engineering systems: a Lyapunov-based approach*. Springer Science & Business Media, 2003.
- [28] M. W. Spong, S. Hutchinson, and M. Vidyasagar, *Robot modeling and control*. John Wiley & Sons, 2020.
- [29] H. K. Khalil, *Control of nonlinear systems*. Prentice Hall, New York, NY, 2002.
- [30] R. Rajamani, *Vehicle dynamics and control*. Springer Science & Business Media, 2011.
- [31] A. Loria, T. I. Fossen, and E. Panteley, “A separation principle for dynamic positioning of ships: Theoretical and experimental results,” *IEEE transactions on control systems technology*, vol. 8, no. 2, pp. 332–343, 2000.

- [32] M. Doff-Sotta, M. Cannon, and M. Bacic, “Optimal energy management for hybrid electric aircraft,” *IFAC-PapersOnLine*, vol. 53, no. 2, pp. 6043–6049, 2020, 21st IFAC World Congress. [Online]. Available: <https://www.sciencedirect.com/science/article/pii/S2405896320322758>
- [33] S. Vedula, K. Omiloli, A. Olajube, and O. Anubi, “Predictive energy management for mitigating load-altering attacks for islanded microgrids using battery energy storage systems,” *ASME Letters in Dynamic Systems and Control*, vol. 6, no. 1, p. 011009, 10 2025. [Online]. Available: <https://doi.org/10.1115/1.4069921>
- [34] M. M. Bijaieh, S. Vedula, and O. M. Anubi, “Model and load predictive control for design and energy management of shipboard power systems,” in *2021 IEEE Conference on Control Technology and Applications (CCTA)*. IEEE, 2021, pp. 607–612.
- [35] C. Weng, J. Sun, and H. Peng, “An open-circuit-voltage model of lithium-ion batteries for effective incremental capacity analysis,” in *Dynamic systems and control conference*, vol. 56123. American Society of Mechanical Engineers, 2013, p. V001T05A002.
- [36] Z. Song, J. Li, J. Hou, H. Hofmann, M. Ouyang, and J. Du, “The battery-supercapacitor hybrid energy storage system in electric vehicle applications: A case study,” *Energy*, vol. 154, pp. 433–441, 2018.
- [37] S. Boyd, N. Parikh, E. Chu, B. Peleato, J. Eckstein *et al.*, “Distributed optimization and statistical learning via the alternating direction method of multipliers,” *Foundations and Trends® in Machine learning*, vol. 3, no. 1, pp. 1–122, 2011.